steel research international
www.steel-research.de

Influence of the Crystallographic Orientation on the Yield Strength and Deformation Mechanisms of Austenitic Grains in Metastable Stainless Steels Investigated by Spherical Nanoindentation

Joan Josep[Q1] Roa,* S. Suarez, H. Yang, G. Fargas, A. Guitar, E. Rayón, I. Green, and A. Mateo[Q2]

The mechanical behavior of a metastable stainless steel is studied by spherical nanoindentation, as a function of crystallographic orientation of their austenitic grains. The residual imprints are analyzed by electron backscattered diffraction (inverse pole figure, phase and geometrically necessary dislocation maps) and atomic force microscopy. Results showed that austenite grains with the most common crystallographic orientations display similar elasto-to-plastic transition, being the dislocation activity by the Frank-Read source the main deformation mechanism. However, the amount of dislocations generated during indentation testing strongly depends on the crystallographic orientation. No evidence of stress-induced phase transformation is observed.

J. J. Roa, G. Fargas, A. Mateo[Q3]
Department of Materials Science and Metallurgical Engineering
Universitat Politècnica de Catalunya
Campus Diagonal Besòs-EEBE
Barcelona 08019, Spain
Centre for Research in Multiscale Engineering of Barcelona
Universitat Politècnica de Catalunya
Campus Diagonal Besòs-EEBE
Barcelona 08019, Spain
E-mail: joan.josep.roa@upc.ed

S. Suarez, A. Guitar
Functional Materials
Department of Materials Science and Engineering
Saarland University
Saarbruecken 66123, Germany

H. Yang, I. Green
G. W. Woodruff School of Mechanical Engineering
Georgia Institute of Technology
30332-0405 Atlanta, USA

E. Rayón
Instituto de Tecnologia de Materiales (ITM)-Universitat Politècnica de València
Valencia 46022, Spain

The ORCID identification number(s) for the author(s) of this article can be found under https://doi.org/10.1002/srin.201800425.

DOI: 10.1002/srin.201800425

1. Introduction

Metastable austenitic stainless steels are used in the production of a wide variety of formed and drawn parts in many industry sectors such as transport, food, or chemical, among others.[1–a] These steels are considered as part of the TRIP (Transformation Induced Plasticity) family, since plastic deformation, either during forming or under service conditions, can lead to strain-induced transformation from austenite to martensite.[4–7] This phase transformation acts as a reinforcing mechanism which makes metastable stainless steels an ideal replacement material to conventional steel grades due to their excellent combination of formability, crash-absorbing capability, and good corrosion resistance.[8] Nevertheless, one major shortcoming lies in the lack of the accurate prediction of their mechanical behavior, because mainly it depends on their microstructure. In metastable stainless steels, the deformation mechanisms typically involve not only linear defects, that is, dislocations, but also planar defects such as stacking faults, shear bands, and mechanical twins,[9,10] as well as the aforementioned phase transformation.[11–13] In this context, the study of the local mechanical properties together with a detailed observation of the plastic deformation mechanisms becomes of utmost importance. In the literature, there are several reports about the study of the mechanical properties of austenitic stainless steels by means of nanoindentation of individual grains.[14,15] Concerning specifically TRIP steels, scarce information is available in the literature.[16–6a] Recently, a work carried out on a metastable stainless steel AISI 301LN demonstrated that the austenite grains displayed an anisotropic behavior with regard to hardness, whereas the elastic modulus remained constant.[38] However, there is still no information available on the deformation mechanisms in the elasto-to-plastic regime.

Within this framework, the purpose of this work is to study the dependence of the crystallographic orientation on the mechanical properties in terms of individual grains, and also at the grain boundary, by spherical nanoindentations. In doing so, advanced characterization techniques such as: Electron Back-Scatter Diffraction (EBSD) and Atomic Force Microscopy (AFM)

are used to analyze the main deformation mechanisms. Moreover, an optimal meshed grid is designed using the finite element analysis (FEA) code, ANSYS, to determine which is the suitable stress field necessary to allow the dislocations to glide until they reach the surface.

2. Experimental Section

The material investigated in this work is a commercial AISI 301LN stainless steel, equivalent to EN 1.4318, supplied by Outokumpu (Finland) as 2 mm thick sheets. Its chemical composition is shown in **Table 1**. Prior to the microstructural and micromechanical characterization, the TRIP steel specimens are polished with silicon carbide and then with diamond suspension of 30, 6, 3, and 1 μm in size. Finally, a neutral suspension of 20 nm alumina particles is used in order to remove possible work hardening introduced during surface preparation. More information is available in ref. [19].

A homogeneous array of 100 imprints (10 by 10) is introduced using a Nano Indenter® XP System (MTS) with continuous stiffness measurement (CSM) having a harmonic displacement of 2 nm and a constant frequency of 45 Hz. The goal is to represent the indentation stress-strain curve ($\sigma - \varepsilon$, see Appendix A), as well as the dislocation motion, as a function of the crystallographic orientation activated under this stress field. The strain rate is held constant at $0.05\,s^{-1}$ along the indentation process. Experiments are performed at room temperature using a spherical diamond tip of 1 μm in radius, and at a maximum displacement into surface of 500 nm. A constant distance of approximately 10 μm is held between each imprint in order to avoid any overlapping effect.

The FEA is used in this work to assist in determining of the minimum required deformation to achieve the indentation-induce plasticity to reach the surface (in terms of dislocations) for the three main austenitic orientations, namely: {001}, {101}, and {111}, more information regarding the FEA is available in Appendix B.

The EBSD analysis, in terms of local crystallographic orientation gradients in deformed austenitic grains, is carried out using a FEI Helios NanoLab Field Emission Scanning Electron Microscope (FE-SEM) operating at 20 keV and 22 nA. EDAX TSL OIM data collection system, with a step size of 30 nm, is used. The data post-processing consisted on the application of a confidence index (CI) standardization routine and filtering of the data possessing a CI below 0.09. Geometrically necessary dislocation (GNDs) density is provided in terms of $10^{-12}\,m^{-2}$, according to the methodology proposed by Field et al.,[20] whose algorithm considers both types of dislocations: edge and screw.

Surface observation of a small region of the homogeneous indentation array, as well as the main deformation mechanisms induced near the residual imprint, are performed by AFM, working in tapping mode. A dimension D3100 microscope from Bruker is used to carry out the different measurements. All the images are processed with the WSxM software.[21]

Table 1. Chemical composition of the studied stainless steel AISI 301 LN (wt%).

	C	Cr	Ni	Mn	Si	Mo	N	Fe
AISI 301 LN	0.02	17.48	7.03	1.23	0.45	0.12	0.12	Bal.

3. Results and Discussion

3.1. Stress–Strain Curve and Flow Stress Anisotropy

Figure 1 exhibits EBSD images of the spherical indentation array of the TRIP stainless steel. The image quality (IQ) map (Figure 1a) allows a qualitative assessment of the grain size, grain deformation close to the residual imprint and pre-existing twins. Furthermore, this image highlights the presence of a bimodal distribution of austenitic grains, with grain mean sizes of 40 ± 5 μm (coarse) and 5 ± 1 μm (fine). Additionally, it is possible to observe some martensitic regions as well as the deformation that these lamellae generated on the austenitic grains (the region is labeled by * in Figure 1a). Figure 1b presents the corresponding local crystallographic or inverse pole figure (IPF) map for the region of interest, where the aforementioned features are also noticeable.

The mean contact pressures (p_m) for the elastic-to-plastic transition as a function of the strain (defined as the ratio between the contact point and the spherical indenter radius, a/R) for three different austenitic grains with a misorientation from the main crystallographic orientations of the austenite grains ({001}, {101}, and {111}) of around 3, 5, and 4°, respectively, are presented in **Figure 2**a. No apparent relationship between phase orientation and mean contact pressure is observed. Three different deformation fields could be clearly distinguished in Figure 2a depending on the contact pressure applied.[22] The first region (linear region, adjusted by a black dash line) corresponds to the zone where $p_m < 1.1 \cdot \sigma_f$, where σ_f is the flow stress. This expression is based on elastically isotropic behavior which is the estimation considered in this situation due to the confining of the residual imprint of individual austenitic grains. Here, the material response is fully elastic. The second region (the point where the experimental points lose the linearity), corresponds to p_m values around $1.1 \cdot \sigma_f$. In this particular point, the plastic deformation occurs near the surface but it is constrained by the surrounding material. Finally, the third region (after the point where the trend loses the linearity and reported in **Table 2**) occurs for values $p_m > 1.1 \cdot \sigma_f$, where the material response is elastic-to-elastoplastic. Specifically, the plastic region extends to the surface of the specimen and continues growing downwards.

Table 2 summarizes the p_m, the flow stress (σ_f), the maximum tensile stress (σ_{tm}), and the maximum shear stress (τ_m) obtained from the equations summarized in Appendix A.

In order to evaluate the anisotropy of the flow stress, Figure 2b shows σ_f values for the analyzed crystal orientations corresponding to the grains observed in the region of study (out of about ten different austenite grains within the referred microstructural EBSD map reported in Figure 1b). Figure 2b presents the flow stress directly determined from the indentation $\sigma - \varepsilon$ curves of austenitic grains as a function of the orientation parameter (o.p.), determined as follows[23]:

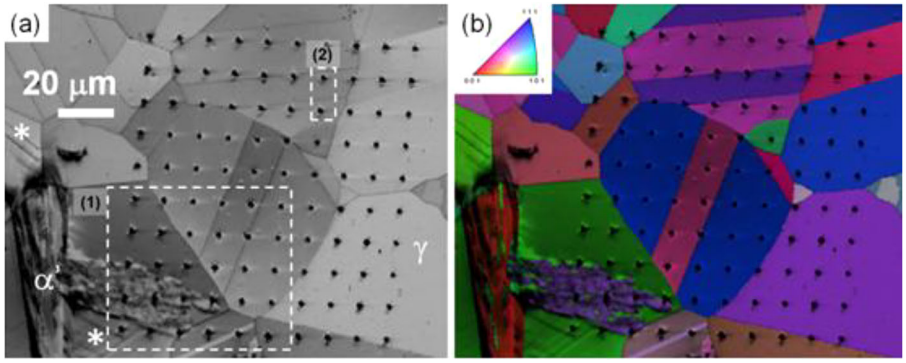

Figure 1. a) Image quality (IQ) and b) Local crystallographic EBSD map or IPF map superimposed to the IQ corresponding to the pre-existing microstructure for the region where the spherical indentation array (10 by 10) is performed for the TRIP stainless steel (pixel size: 30 nm).

$$o.p. = 3\frac{h^2k^2 + k^2l^2 + l^2h^2}{(h^2+k^2+l^2)} \quad (1)$$

where h, k, and l are the Miller indices from each grain, and they are obtained through the Euler's angles as directly determined from the EBSD measurements. The *o.p.* near 0 corresponds to grains oriented to the {001} plane, whereas *o.p.* around 1 are related to the {111} plane.

From the data summarized in Table 2 and extracted from Figure 2a, the role of the crystallographic orientations on the mechanical properties determined from the indentation curves is unclear for the {001} and {101} planes. Additionally, the {111} planes present slightly higher values than those reported for the other planes. Furthermore, as seen in Figure 2b, the flow stress is isotropic, with a constant value ranged between 1.1 and 1.3 GPa. The σ_f values reported in Table 2 are in agreement with those determined through the micropillar compressions tests on TRIP stainless steel.[19]

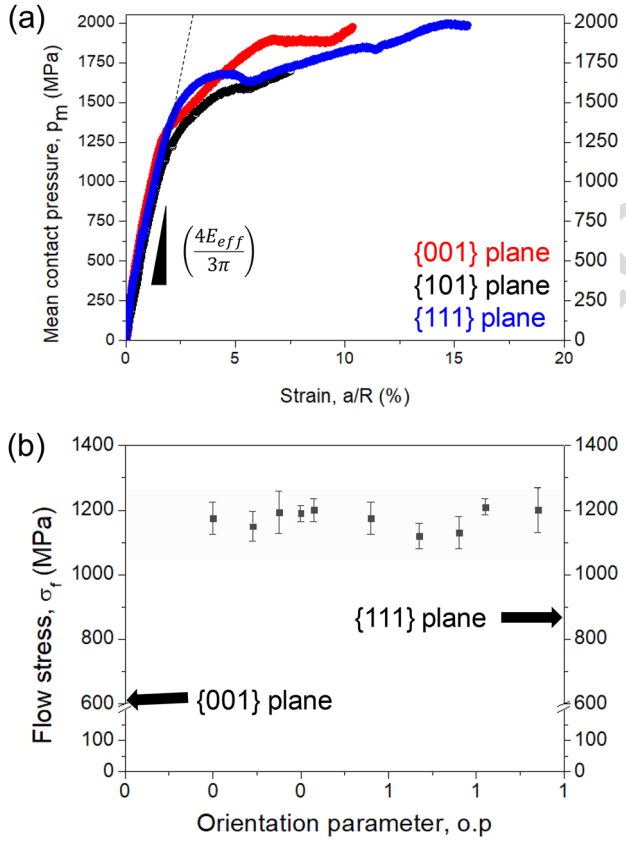

Figure 2. a) Representation of the indentation stress-strain ($\sigma - \varepsilon$) curves only for the main crystallographic orientations (other curves for the different crystallographic orientations investigated here are not shown in Figure 3a); and b) the flow stress (σ_f) directly extracted from the indentation stress-strain curves as a function of the orientation parameter (o.p).

3.2. Plastic Deformation Mechanisms Induced by Spherical Indentation

By using the FEA it is possible to estimate the minimum penetration depth required by the indenter for the dislocations activated by the plastic field to reach the surface, as shown in Figure 3 (see white arrow). It is found that this value is independent of the austenitic crystallographic orientation, and around five times the ω_c, which ranges between 1.230 and 0.734 μm for {001} and {111}, respectively. This observation is in close agreement with the FEA information of elasto-plastic hemispherical contact against a rigid flat, as reported in ref. [24]. However, the value predicted by the FEA does not fits with the value experimentally used due to a simple isotropic, 2D FEA

Table 2. Mean contact pressure (p_m), flow stress (σ_f), maximum tensile stress (σ_{tm}), and maximum shear stress (τ_m) for the main crystallographic orientations.

Crystallographic orientation	p_m [MPa]	σ_f [MPa]	σ_{tm} [MPa]	τ_m [MPa]
{001}	1251	1137	213	575
{101}	1274	1158	217	586
{111}	1407	1279	239	647

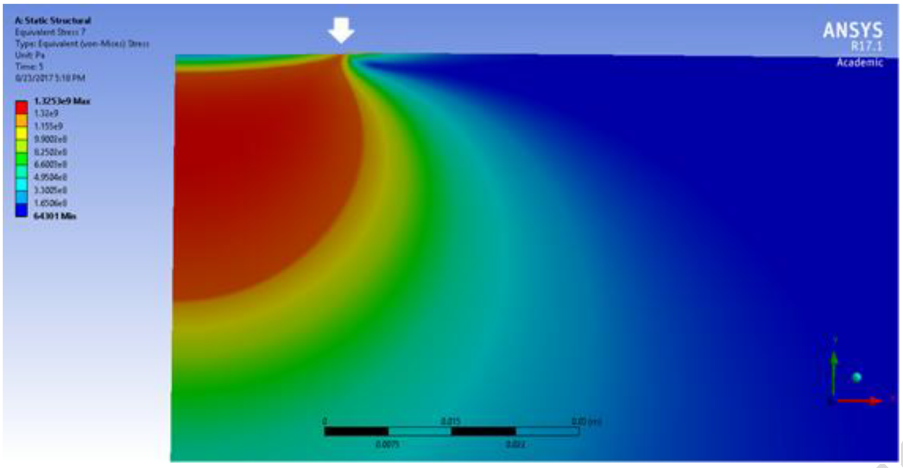

Figure 3. Representation of the Von Misses stress for the {001} austenitic grain, when the first plastic field reaches the surface.

model of the nanoindentation of austenite crystals proved insufficient for determining when plastic deformation reaches the surface. Despite the indentation response not showing a strong dependence on crystal orientation (i.e., {100} vs. {111}), simulations require an elastically and plastically anisotropic material model to provide a meaningful estimation of when the plastic deformation at the indentation site reaches the surface.

Within this context, **Figure 4** shows a set of AFM images (left hand side) of several residual spherical imprints (corresponding to the white dash square in Figure 1a). A pre-existing *α'*-martensitic lamella can be clearly distinguished as well. The plastic field induced by the spherical nanoindentations is recognizable near the residual imprints. The same figure (the right hand side) depicts 3D-AFM magnified images for several residual imprints (white dash squares in the error signal mode image on the left hand side). As it is evident for all the spherical imprints, deformation-related features are present. These features are aligned with {111} traces. Furthermore, these lineal marks may be associated with slip traces activity induced during the indentation process. As can be observed for the imprint performed inside the *α'*-martensite lamella (imprint 3) the dislocation activity is smaller compared with the imprints performed in the austenitic phase (imprints 1, 2, and 4). This difference may be related with a different crystallographic structure between both phases, emphasizing the effect of the crystallographic orientation on the deformation behavior. The residual imprint labeled (4) presents several pre-existing twins. It is reasonable to state that these pre-twins (also observed in Figure 1a) are generated during the industrial manufacturing process, and may be due to the residual stresses induced during the steel solidification. These stresses are related to the different thermal expansion coefficients between the austenitic and the *α'*-martensitic phases, varying between 2 and 3.1%, as reported Moyer et al.[25] for iron-carbon alloys.

Attempting to get a more detailed insight on the induced deformation scenario and the crystallographic orientation relationship, high resolution EBSD maps (GND, IPF and phase maps, see **Figure 5**b) are investigated for 16 residual spherical imprints, marked as a white dashed square in the IQ image (Figure 5a). From those, it is possible to thoroughly analyze the

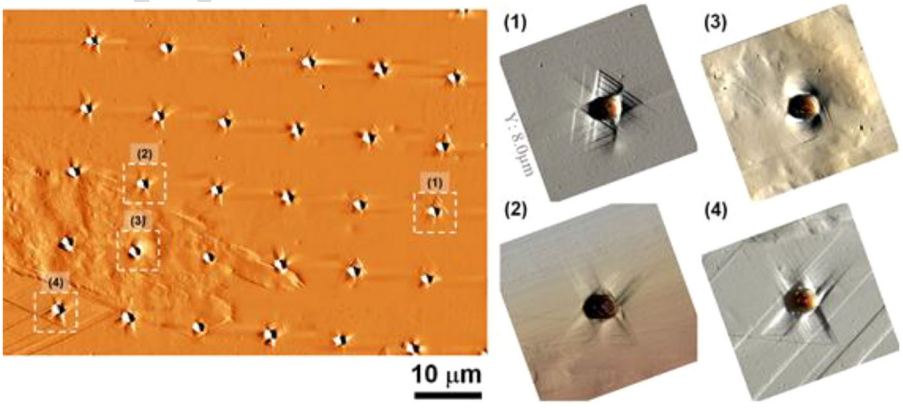

Figure 4. Set of AFM images (error signal mode image, left side) showing the main plastic deformation mechanisms around the residual imprints for region (1) delimited with a dash square line in the IQ map (Figure 2a) and a 3D magnified AFM images (right side) of four different spherical imprints (labeled (1) to (4) in the error signal mode image).

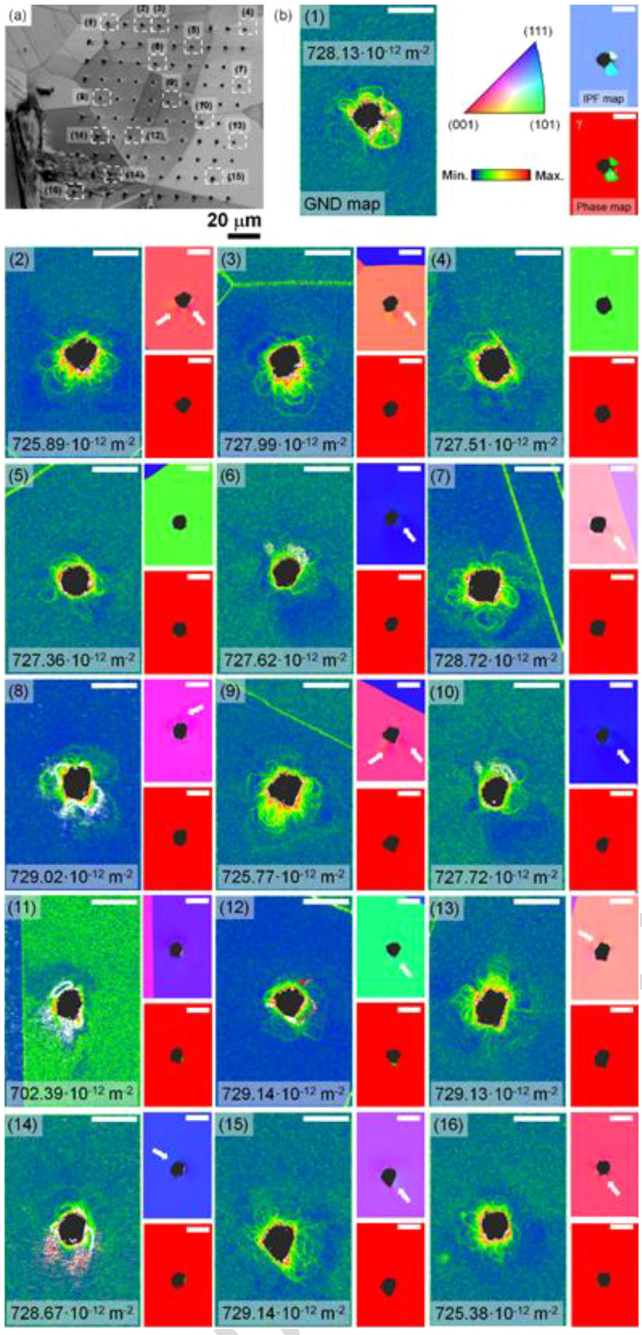

Figure 5. a) IQ of the spherical indentation array (Figure 2a); the dash white squares exhibit the residual imprints which are observed in detail. GNDs, IPF and phase maps are presented in b) for sixteen different spherical imprints. In the phase maps, red and green colors correspond to austenitic and martensitic phases, respectively. Each scale bar corresponds to 2 μm.

plastic deformation mechanisms induced under the stress field created by applying spherical nanoindentations.

The color maps (Figure 5b) show the GND distribution. Here, the average misorientation of an EBSD point is calculated with respect to the second nearest neighbors (values above 5° are considered grain boundaries and, thus, are excluded from the analysis). As expected, under the influence of the applied stress the GND pile-up and, as a consequence, the maximum density of GNDs (around 10^{-14}–10^{-15} m^{-2}) is located at the vicinity of the spherical imprints (mainly at the contact point between the indenter and the material, where the stress field induced during the indentation process is maximum). The maximum dislocation density activated under this stress field and near the residual imprints varies between $702 \cdot 10^{-12}$ and $729 \cdot 10^{-12}$ m^{-2}. Within this context, the dislocation activity can be considered dependent upon the crystallographic orientation. However, this difference is not significantly large enough to support an anisotropic parameter, since a simple relationship does not exist between regions of high GND content and the crystallographic orientation, or even between the grain size.

It should be noted that the dislocation distribution presented by the GND maps lead to the understanding of the

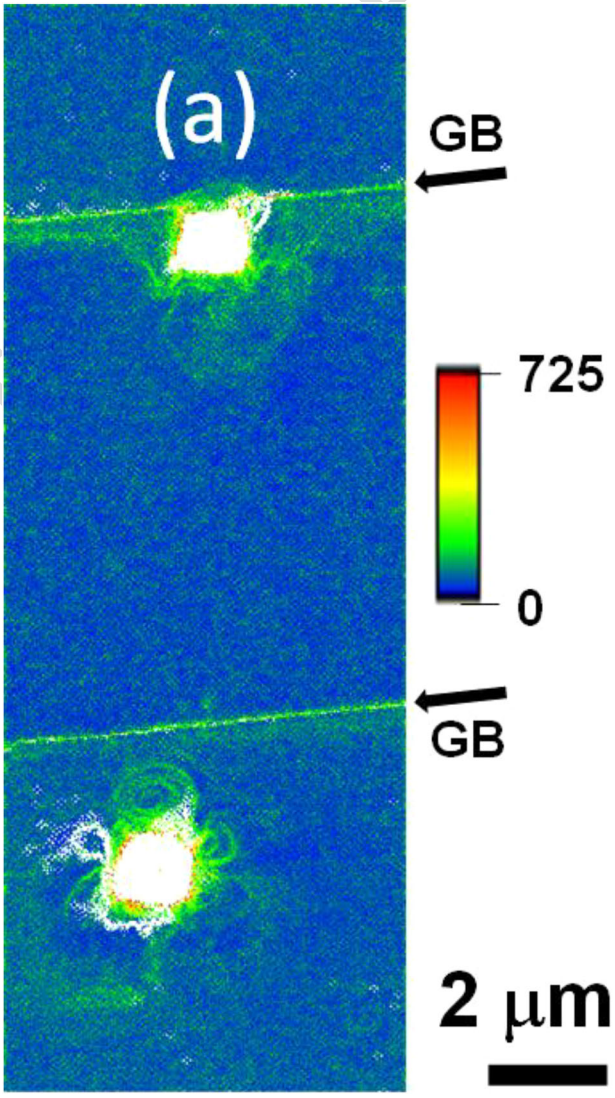

Figure 6. GND map of two residual imprints performed in two different crystallographic austenitic grains (labeled as (2) in Figure 2a) showing the dislocation map induced during the indentation process. Two black arrows show two different austenitic grain boundaries (GBs).

accommodation of the plastic deformation induced during the indentation process. In addition, the distribution of GND density near the residual imprints seems to be uniform, since most of the values considered for the calculation are slightly lower than 5°. The 2D analysis of GNDs maps (see Figure 5b) also revealed important information about the inhomogeneous in-grain accommodation of the deformation induced by the spherical indentations in different austenitic crystallographic grains.

Furthermore, as it is evident for mainly all the residual imprints observed in this work by using this methodology, the main deformation mechanisms are associated to the multiplication of dislocations by Frank-Read sources, as described in ref. [26]. Moreover, when the indentation is performed near a grain boundary, the dislocation sources are blocked by its presence, acting as a discontinuity between two different austenitic grains. This feature is clearly observed in the spherical imprint labeled as (7) in Figure 5b. The same phenomenon is observed in **Figure 6** for a pair of imprints labeled as (2) in Figure 1a. In this particular case, both imprints are done in two different austenitic crystallographic orientations, where the maximum dislocation density is found to be around $725 \cdot 10^{-12}$ m^{-2}. As it is evident in the GND map, the maximum density is accumulated at the contact point between the spherical indenter and the material, as previously explained in Figure 5b.

Phase orientation maps for all the spherical imprints are also shown in Figure 5b, revealing that the stress field induced during the indentation process does not produce the aforementioned phase transformation. However, the phase map for the imprint (1) discloses a marked dislocation pile-up near the residual imprint (in agreement with ref. [27]), being likely related to the phase transformation in the deformed region and implying a volume expansion ranged between 1 and 4%. This can be due to the fact that this particular crystallographic orientation, between the {111} and {101} plane, favors the phase transformation. It is necessary to note that this observation has been previously reported at the macroscopic length scale,[28] as well as at the micrometric length scale under different stress fields.[19,29,38] On the other hand, this trend is only evident for one of the spherical imprints (imprint (1) in Figure 5b); which implies that for the others, the stress induced during the indentation process is not large enough to induce phase transformation.

Finally, a slight rotation of the crystallographic structure is evidenced about some residual spherical imprints (which are marked with white arrows in the IPF images in Figure 5b). Such effect may be related to the accumulation of residual stresses derived from the indentation process, and may result in a gradual change in the loading indentation axis during the loading scenario, as predicted by Zaafarani et al.[30] and in agreement with other works published on TRIP steels by Roa et al.[38]

To better understand the dislocation activity near the pre-existing martensite, a detailed EBSD observation is presented in **Figure 7**. A high dislocation density is clearly observed at the interface between austenitic and martensitic grains (Figure 7a). For the particular case in which the imprint lies in the pre-existing martensite lamella (Figure 7c), a pile-up of dislocations around the residual imprint as well as the grain rotation is evident in Figure 7b. This is the same effect as that previously explained in detail in Figure 4b.

The observation of the residual imprints presented from Figure 4–6, indicates that deformation in TRIP steels, under this particular field stress, is predominantly governed by slip activity rather than by phase transformation if we only take into consideration the local behavior of the austenitic grains. The operating deformation mechanism depends on the stacking

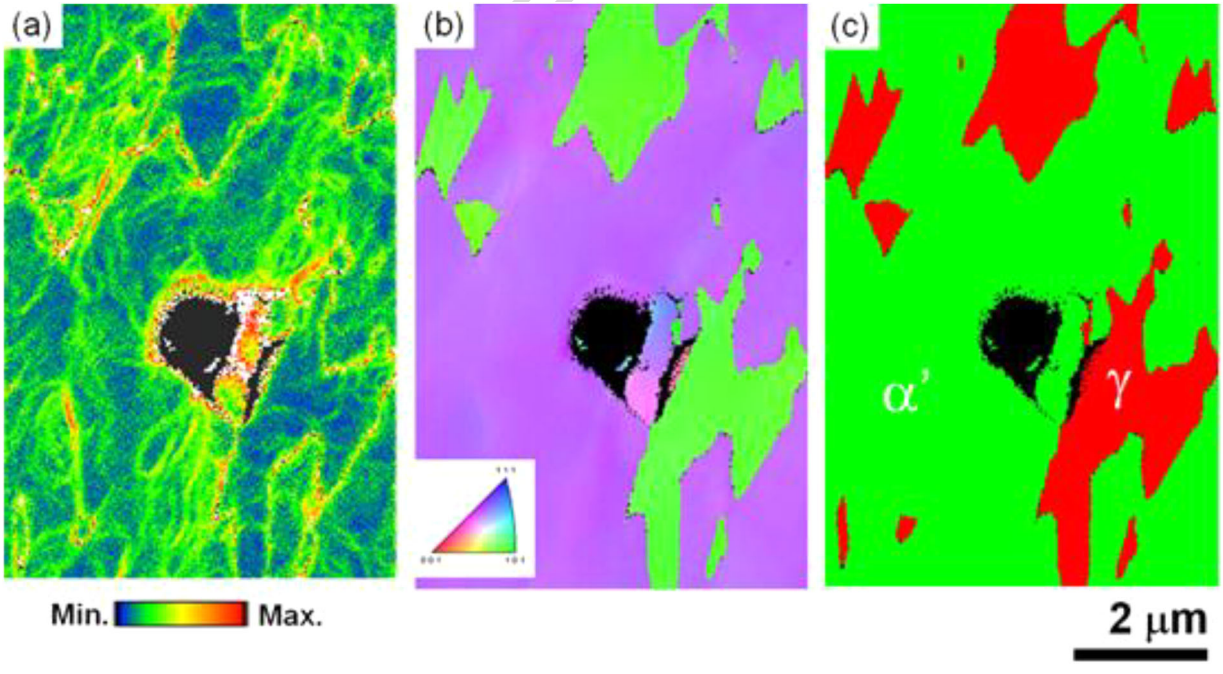

Figure 7. a) GND map of a residual spherical imprint performed at the vicinity of a martensite lamellae showing the dislocation map, b) IPF map, and c) phase map (in red the austenitic, γ, phase and in green the martensitic, α'). Step size is held constant and equals to 30 nm.

fault energy (SFE), being the main parameter controlling the activation of the different deformation mechanisms. Moreover, this parameter also plays an important role in determining the austenitic stability, since it controls the formation of shear bands, and subsequently, the nucleation sites for the martensite.

Using the equation proposed by Schramm and Reed,[31] SFE can be determined as follows:

$$\mathrm{SFE} = -53 + 6.2(\mathrm{Ni}) + 0.7(\mathrm{Cr}) + 3.2(\mathrm{Mn}) + 9.3(\mathrm{Mo}) \quad (2)$$

where SFE is in mJ m^{-2} and the elements are in mass%. The value of SFE for the AISI 301LN studied steel is calculated to be 7.87 mJ m^{-2}. Since this SFE value is lower than the threshold to induce phase transformation (around 13 mJ m^{-2}), it is expected that the dislocations induced during indentation are dissociated to partial Schockley dislocations. These two partial dislocations are then bound together by the stacking fault, and will move together as a unit along the slip plane, as reported Karjalainen et al.[32] and experimentally observed by Roa et al.[33]

4. Conclusions

In this study, spherical nanoindentation tests arrays in a metastable austenitic stainless steel AISI 301LN are performed in order to evaluate the yield strength values as a function of the crystallographic orientation and to analyze the main deformation mechanisms by using complementary high resolution techniques. The following conclusions are drawn:

1) The elastic-to-plastic transition occurs at the same range of the mean contact pressure, between 1251 and 1407 MPa, for {001} to {111} studied crystallographic orientations. In terms of the maximum tensile stress, the corresponding values are 1137 and 1279 MPa, for the aforementioned orientations, respectively.
2) The accommodation of the dislocations is inhomogeneous within the austenitic grains, depending on the crystallographic orientation. Moreover, it differs from the case when the imprint is located at the grain boundaries. GND-map analysis pointed out that the amount of stored dislocations is independent on the crystallographic orientation.
3) The main mechanism of plastic deformation takes place through dislocation activity by the movement of a Frank-Read source.
4) Plastic deformation caused by spherical nanoindentation at the studied conditions rarely leads to the formation of stress-induced *α'*-martensite.
5) The values obtained from this preliminary FEA analysis do not correctly fit with the observed ones because the hypotheses used (e.g., 2D-axysimmetric rigid sphere and isotropic model) are not appropriated. In this sense, a 2D isotropic model is insufficient to determine the minimum material displacement required to displace one dislocation line.

Supporting Information

Supporting information is available from the Wiley Online Library or from the author.

Acknowledgements

The authors acknowledged the financial support from the Spanish Government through the project MAT2015-70780-c4-3-P. S. S., A. G. and F. M. acknowledged the EFRE Funds of the European Commission for support of activities within the AME-Lab project. This work was supported by the CREATe-Network Project, Horizon 2020 Program of the European Commission (RISE Project Nr. 644013). J.J. Roa acknowledged the Serra Hunter programme of the Generalitat de Catalunya.

Conflict of Interest

The authors declare no conflict of interest.

Keywords

electron backscattered diffraction, finite element analysis, metastable stainless steels, nanoindentation, spherical indentation

Received: August 6, 2018
Revised: February 7, 2019
Published online:

[1] J. Yan, M. Gao, X. Zeng, *Opt. Laser Eng.* **2010**, *48*, 512.[Q4]
[2] S. Rajasekhara, L. P. Karjalainen, A. Kyröläinene, P. J. Ferreira, *Mater. Sci. Eng. A* **2010**, *527*, 1986.
[3] H. F. G. De Abreu, M. J. G. Da Silva, L. F. G. Herculano, H. Bhadeshia, *Mater. Res.* **2009**, *12*, 291.
[4] J. B. Vogt, Z. Magnin, J. Foct, *Fatigue Fract. Eng. Mater. Struct.* **1993**, *16*, 555.
[5] G. Fargas, J. J. Roa, A. Mateo, *Mater. Sci. Eng. A.* **2015**, *641*, 290.
[6] G. Fargas, J. J. Roa, A. Mateo, *Wear* **2016**, *364–365*, 40.
[7] D. F. Martelo, A. Mateo, M. D. Chapetti, *Int. J. Fatigue* **2015**, *77*, 64.
[8] R. Andersson, C. Magnusson, E. Schedin, in: *Proceedings of the Conference of the Second Global Symposium on Innovations in Materials Processing and Manufacturing, Sheet Materials*, TMS, NewOrleans, February 11–15, **2001**.
[9] S. Taheri, A. Hauet, L. Taleb, C. Kpodekon, *Int. J. Plast.* **2011**, *27*, 1981.
[10] J. Talonen, H. Hänninen, *Acta Mater.* **2007**, *55*, 6108.
[11] K. H. Lo, C. H. Shek, J. K. L. Lai, *Mater. Sci. Eng. R. Rep.* **2009**, *65*, 39.
[12] T. Byun, E. Lee, J. Hunn, *J. Nucl. Mater.* **2003**, *321*, 29.
[13] T. Kruml, J. Polák, S. Degallaix, *Mater. Sci. Eng. A* **2000**, *293*, 275.
[14] C. Tromas, J. C. Stinville, C. Templier, P. Villechaise, *Acta Mater.* **2012**, *60*, 1965.
[15] M. D. Taylor, K. S. Choi, X. Sun, D. K. Matlock, C. E. Packard, L. Xu, F. Barlat, *Mater. Sci. Eng. A* **2014**, *597*, 431.
[16] T.-H. Ahn, C.-S. Oh, D. H. Kim, K. H. Oh, H. Bei, E. P. George, H. N. Han, *Scr. Mater.* **2010**, *63*, 540.
[17] Q. Furnémont, M. Kempf, P. J. Jacques, M. Göken, F. Delannay, *Mater. Sci. Eng. A* **2002**, *A328*, 26.
[18] D. Tjahjanto, S. Turteltaub, A. Suiker, S. Van Der Zwaag, *Adv. Eng. Mater.* **2009**, *11*, 153.
[19] J. J. Roa, J. M. Wheeler, T. Trifonov, G. Fargas, A. Mateo, J. Michler, E. Jiménez-Piqué, *Mater. Sci. Eng. A* **2015**, *647*, 51.
[20] D. P. Field, P. B. Trivedi, S. I. Wright, M. Kumar, *Ultramicroscopy* **2005**, *103*, 33.
[21] I. Horcas, R. Fernández, J. M. Gómez-Rodríguez, J. Colchero, J. Gómez-Herrero, A. M. Baro, *Rev. Sci. Instr.* **2007**, *78*, 013705/1.
[22] A. C. Fisher-Cripps, *Nanoindentation*, 2nd ed., Vol. *3*, Springer-Verlag Press, New York, USA **2004**, pp. 9–10.

[23] U. Müller, *Applications of Crystallographic Group Theory in Crystal Chemistry*, Oxford Science Publications, UK, ISBN 978-0-19-966995-0, **2013**.
[24] R. L. Jackson, I. Green, *J. Tribol*. **2005**, *127*, 343.
[25] J. M. Moyer, G. S. Ansell, *Met. Trans. A* **1975**, *6A*, 1785.
[26] D. Hull, D. J. Bacon, *Introduction to Dislocations*, 4th ed., Elsevier Ltd. ISBN: *978-0-08-096672-4*, **2001**.
[27] R. F. Bunshah, R. F. Mehl, *Trans. AIME* **1953**, *197*, 1251.
[28] J. Venables, *Philos. Mag*. **1962**, *7*, 35.
[29] I. Sapezanskaia, J. J. Roa, G. Fargas, M. Turon-Viñas, T. Trifonov, R. K. Njiwa, A. Redjaïmia, A. Mateo, *Mater. Charact*. **2017**, *131*, 253.
[30] N. Zaafarani, D. Raabe, F. Roters, S. Zaefferer, *Acta Mater*. **2008**, *56*, 31.
[31] A. Di Schino, M. Barteri, J. M. Kenny, *J. Mater. Sci. Lett*. **2002**, *21*, 751.
[32] L. P. Karjalainen, T. Taulavuori, M. Selliman, A. Kyröläinen, *Steel Res. Int*. **2008**, *79*, 404.
[33] J. J. Roa, G. Fargas, E. Jiménez-Piqué, A. Mateo, *Mat. Sci. Eng. A* **2014**, *597*, 232.
[34] A. J. Moseson, S. Basu, M. W. Barsoum, *J. Mater. Res*. **2008**, *23*, 204.
[35] E. Jiménez-Piqué, Y. Gaillard, M. Anglada, *Key Eng. Mater*. **2007**, *333*, 107.
[36] S. Basu, A. Moseson, M. W. Barsoum, *J. Mater. Res*. **2006**, *21*, 2628.
[37] W. C. Oliver, G. M. Pharr, *J. Mater. Res*. **1992**, *7*, 1564.
[38] W. C. Oliver, G. M. Pharr, *J. Mater. Res*. **2004**, *19*, 3.
[39] B. R. Lawn, *J. Am. Ceram. Soc*. **1998**, *81*, 1977.
[40] J. J. Roa, G. Fargas, A. Mateo, E. Jiménez-Piqué, *Mater. Sci. Eng. A* **2015**, *645*, 188.
[41] I. Green, *Int. J. Appl. Mech. Eng*. **2005**, *10*, 451.

J. J. Roa,* S. Suarez, H. Yang, G. Fargas, A. Guitar, E. Rayón, I. Green, A. Mateo 1800425

Influence of the Crystallographic Orientation on the Yield Strength and Deformation Mechanisms of Austenitic Grains in Metastable Stainless Steels Investigated by Spherical Nanoindentation

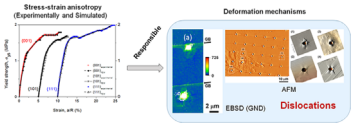

Mechanical behavior of a metastable stainless steel is studied by spherical nanoindentation as a function of crystallographic orientation. Residual imprints are analyzed by EBSD and AFM. Results show that austenite grains with different crystallographic orientations display similar trend, being the Frank-Read source the main deformation mechanisms. No evidence of stress-induced phase transformation is observed.